An Energy-Based Model of Four-Switch Buck-Boost Converters

Ezio Gallo, *Student Member, IEEE*, Davide Biadene, *Member, IEEE*, Filip Cvejić, *Student Member, IEEE*, Giorgio Spiazzi, *Member, IEEE*, Tommaso Caldognetto, *Senior Member, IEEE*

***Abstract*—The four-switch buck-boost (FSBB) topology is often used in combination with other isolated converters to extend the voltage range capability of the overall structure. In such applications, the duty-cycles of the two legs of the FSBB are independently controlled, and a phase-shift is typically used to shape the inductor current ripple and thus achieve zero voltage switching. This paper proposes a non-linear average model, and the corresponding linearized small-signal model for the FSBB operating in the described way. Notably, the proposed approach is based on the modeling of the inductor energy, which allows the correct description of the dynamics related to the phase-shift, in addition to those related to the duty-cycles. The derived models are shown to be in excellent agreement with simulation results and are also validated by measurements on an experimental prototype.**

***Index Terms*—four-switch buck-boost, average model, small-signal model.**

I. INTRODUCTION

THE four-switch buck-boost (FSBB) topology, shown in Fig. 1, is a well-known non-inverting step-up/down topology, which is used in combination with other isolated converters for higher input/output voltage ranges. In [1], an integrated buck-boost LLC converter (IBBL) is proposed, cascading an FSBB stage and an LLC stage with passive rectification sharing a switching leg to widen the input voltage range. The LLC stage works in zero current switching (ZCS) operation throughout the full operating range. Here, the two stages are driven independently with different switching frequencies for the two legs. The same converter is used in [2] as intermediate bus converter in distributed telecom power systems. The legs of the FSBB work at the same switching frequency and the shared leg operates at 50% duty-cycle. The output voltage is regulated by the input-leg duty-cycle. The phase-shift is modulated to reduce the current ripple in the buck-boost inductor. Similarly, in [3] and [4], the converter is used with push-pull rectifier and full-bridge rectifier, respectively, with the bipolar symmetric phase-shift modulation. In these applications the shared leg duty-cycle is fixed at 50% and the duty-cycle of the other leg and the phase-shift are modulated to regulate the output voltage and modify the inductor current. In [5], a parallel structure using two interleaved FSBB stages working in counter-phase is also proposed. The FSBB is used with a dual active bridge (DAB) converter to match the high and low voltage side reducing, in this way, the current stress and increasing the soft-switching range [6]. Other articles emphasise the fundamental role of the FSBB as front-end stage in unidirectional dc-dc converters [7]–[11] or as an additional stage in power factor correction or in bidirectional converters, widening the converter voltage range and eventually improving the efficiency of the other stage in a wide range of operation [12], [13].

Despite the simple structure of the FSBB, models covering the dynamics of the converter during the variation of both the two duty-cycles and the phase-shift are not presented. Typical FSBB average models account for buck or boost operating modes, where only one of the legs is modulated to reach the desired output voltage, or operating in buck-boost mode where S_1 and S_3 of Fig. 1 are turned on and off simultaneously. When these operating modes are considered, as in [14]–[16], the canonical method in [17] is generally used neglecting the dynamics of the converter in the transition between the buck and boost mode of operation in the so called dead zone. In [18], a quadrangle current control for the FSBB is presented and, in [19], a model of the converter under that control is developed, considering the variation of the duty-cycles and the phase-shift. With such a control, since the minimum current to reach ZVS operation is fixed, one of the three variables (i.e., the two duty-cycles or the phase-shift) become dependent to the others, limiting the validity of the model.

The transition between the buck and boost modes is considered in several papers. In [20], control strategies utilizing buck-boost operation are employed for a smooth transition between the modes. The strategy proposed in [20] is used also in [21] and [22], changing the overlap between the carrier of the switches S_1 and S_2 to gently reduce one duty-cycle and increase the other, effectively changing the phase-shift. However, a single small-signal model for the FSBB in all the three operation modes (i.e., buck, boost and buck.boost modes) is derived and the effect of the phase-shift, present in the buck-boost mode, is neglected. On the other hand, in the literature, the phase-shift dynamic is considered in other converter topologies such as the dual half bridge (DHB) or DAB [23]–[26] in which, however, the phase-shift is used to change the power transferred at the output.

The aim of this paper is to develop a non-linear average

E. Gallo, D. Biadene, and T. Caldognetto are with the Department of Management and Engineering, University of Padova, Vicenza, Italy (e-mail: ezio.gallo@phd.unipd.it, tommaso.caldognetto@unipd.it, davide.biadene@unipd.it). F. Cvejić, and G.Spiazzi are with the Department of Information Engineering, University of Padova, Padova, Italy (e-mail: filip.cvejic@unipd.it, giorgio.spiazzi@unipd.it).

This article has been accepted for publication in IEEE Transactions on Power Electronics. This is the author's version which has not been fully edited and content may change prior to final publication. Citation information: DOI 10.1109/TPEL.2023.3349327

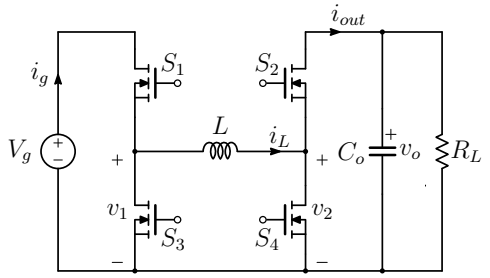

Fig. 1: Four-switch buck-boost (FSBB) converter.

model for the converter in Fig. 1 in the most general case where both input and output legs operate with independent duty-cycles, and considering the effect of the phase-shift between the two legs.

From the non-linear average model, a simple linearization technique is used to derive the desired small-signal linear model.

This paper develops on the preliminary results reported in [27]. Herein, the theoretical treatment is enhanced by performing the analysis based on a general energy modeling of the converter. Moreover, additional results are reported, including phase-shift perturbations, comparisons with average state-space models, and validations comprising all the switching patterns. The proposed modeling approach, besides encompassing effects of variables like the input and output duty-cycles, akin to other average modeling approaches in the literature, it also allows the modeling of the converter behavior in response to phase-shift variations, which is typically not included in common models, as also elaborated in other research papers (see, e.g, [19]).

In the following, Sect. II, the converter modes of operation are reviewed. Sect. III presents the energy-based approach and shows the derivation of the average and small-signal models of the converter. In Sect. IV, the modeling approach is verified by simulations in Matlab/Simulink also providing a control application example. Sect. V reports the experimental validation. Sect. VI concludes the paper.

II. Review of the FSBB operating modes

The main waveforms of the FSBB converter are displayed in Fig. 2. D_g and D_o are defined as the duty-cycles of the top switch of the input and output legs respectively, denoted as S_1 and S_2 in Fig. 1. The phase-shift β is defined as the relative time between the center instants of the voltage pulses of v_1 and v_2 and it is positive when v_2 leads v_1.

From the volt-second balance of the inductor, the voltage gain is derived as a function of the two duty-cycles. Thus, the phase-shift β can be used to shape the piece-wise linear current waveform i_L to achieve ZVS for the four switches as well as to minimize its RMS value. Depending on the phase-shift β, four different modes are possible for each of the step-up or step-down cases.

In these operating regions the switching period can be divided into four different sub-periods Δt_k bounded by the leg commutation instants t_k, as shown in Fig. 2. In (1), the sub-periods Δt_k and their normalized duration δ_k are described

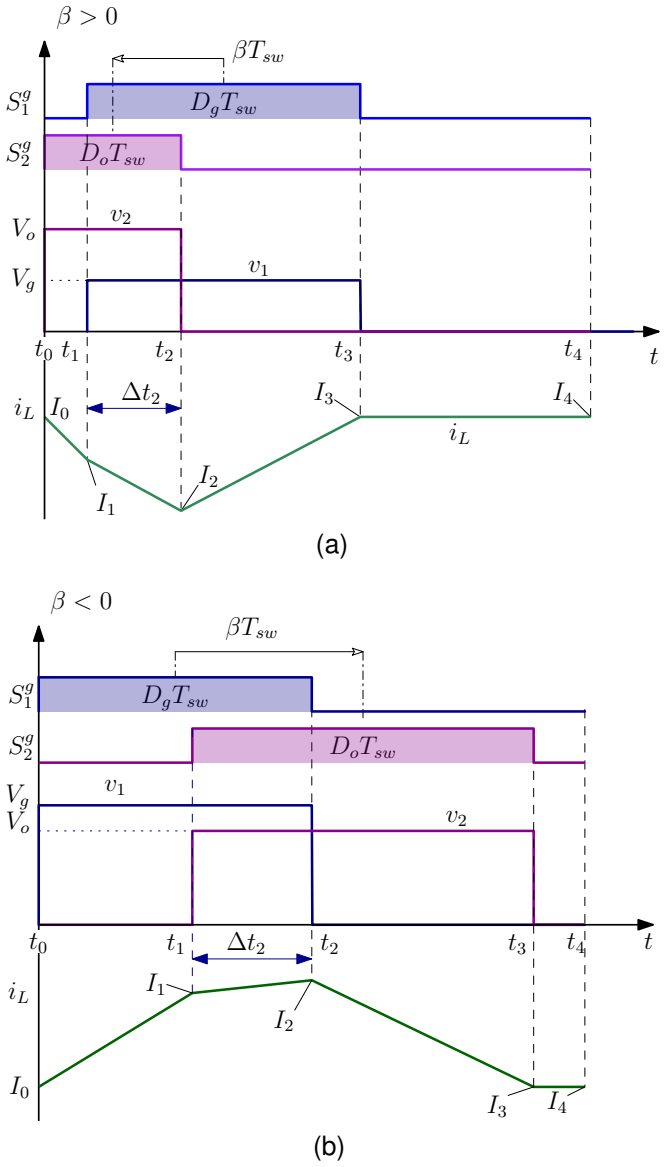

Fig. 2: Example of converter waveforms for different phase-shift values. (a) Region $\mathcal{R}2$ in step-up case (i.e., $D_o < D_g$); (b) region $\mathcal{R}8$ in step-down case (i.e., $D_o > D_g$).

as a function of the two duty-cycles, D_g and D_o, and the phase-shift β.

$$\Delta t_k = t_k - t_{k-1} \quad \Rightarrow \quad \delta_k = \frac{\Delta t_k}{T_{sw}} = f(D_g, D_o, \beta). \quad (1)$$

The boundaries of the operating modes are dependent on the defined quantities D_g, D_o, and β. Each boundary satisfies the particular condition $\delta_k = 0$ defining an hyperplane in the (D_g, D_o, 2β)-space. The resulting space-partition defines the different converter modes. The expressions of the intervals δ_k are shown in Table I for the regions $\mathcal{R}4$-8 (i.e., $\mathcal{R}4$ and $\mathcal{R}8$).

A graphical representation of the operating regions is reported in Fig. 3, where they are evaluated for D_g equal to 0.4 and 0.6. This allows to project the space-partition on the (D_o, 2β)-plane.

Given the intervals definition in (1), the corresponding

This article has been accepted for publication in IEEE Transactions on Power Electronics. This is the author's version which has not been fully edited and content may change prior to final publication. Citation information: DOI 10.1109/TPEL.2023.3349327

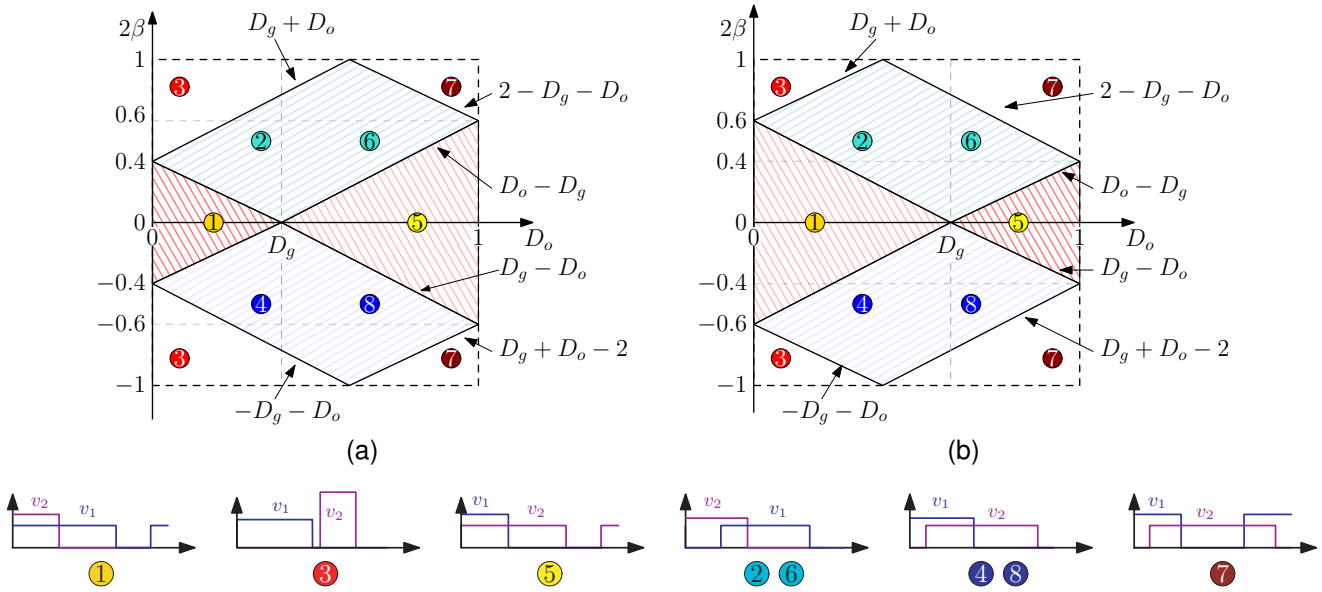

Fig. 3: Mode boundaries for different input duty-cycles. (a) $D_g = 0.4$; (b) $D_g = 0.6$. The different switching pattern are reported above.

TABLE I: Normalized time interval equations for the region $\mathcal{R}$4-8

Interval	Expression	Interval	Expression
δ_1	$\frac{D_g}{2} - \frac{D_o}{2} - \beta$	δ_3	$-\frac{D_g}{2} + \frac{D_o}{2} - \beta$
δ_2	$\frac{D_g}{2} + \frac{D_o}{2} + \beta$	δ_4	$1 - \frac{D_g}{2} - \frac{D_o}{2} + \beta$

inductor current at the instant t_k [i.e., $I_k = i_L(t_k)$] can be described by:

$$I_k = I_{k-1} + \frac{\Delta t_k}{L} V_{Lk}, \quad k = 1, 2, 3, 4, \tag{2}$$

where V_{Lk} is the voltage across the inductor L during the k-th sub-period. Iterating (2) for all the intervals Δt_k, all the switching current values I_k are found with respect to I_0.

In this paper, the analysis is focused on regions $\mathcal{R}$4-8 and $\mathcal{R}$2-6 since they allow ZVS turn-on transitions for all four switches by modulating the phase-shift. Operation in regions $\mathcal{R}$1-5 precludes complete ZVS and is, thus, typically avoided.

In the following, the use of the overlap interval δ_2 as a control variable is preferred over β.

III. Energy-Based Modeling

A. Limitation of Average Quantities on a Switching Period

Let us first consider an example to highlight a limitation of considering a model based on the average quantities computed over a generic switching period. To this end, the modeling of the effect of a phase-shift variation is analyzed in the following.

Fig. 4 displays the main waveforms of an FSBB converter when a phase-shift variation is applied while keeping constant the duty-cycles D_g and D_o. The change of the v_1-v_2 overlap

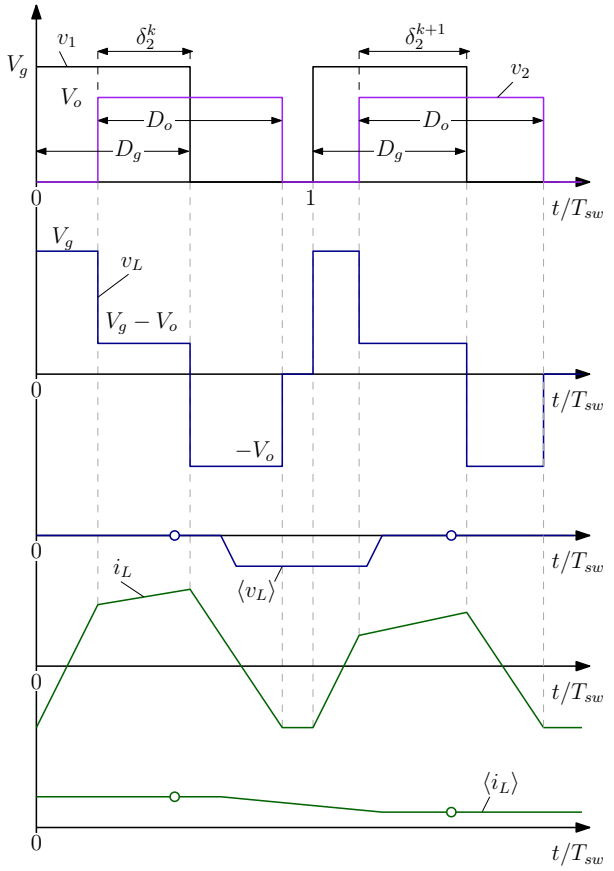

Fig. 4: Instantaneous and moving average waveforms in $\mathcal{R}$4-8. A variation in the overlap δ_2 generates a step response on the voltage $\langle v_L \rangle$ that causes a variation on the inductor current i_L and thus in its moving average $\langle i_L \rangle$. Circles $\circ$ mark the values of the average quantities computed on a switching period.

(i.e., δ_2) causes a variation in the average inductor current $\langle i_L \rangle$, where the function $\langle x \rangle$ is the moving average of the signal x:

$$\langle x \rangle(t) = \frac{1}{T_{sw}} \int_{t-\frac{T_{sw}}{2}}^{t+\frac{T_{sw}}{2}} x(\tau) d\tau. \tag{3}$$

The variation observed in $\langle i_L \rangle$ is expected and should correspond to an associated variation in the modeled average inductor voltage. However, commonly used average models of FSBBs approximate $\langle v_L \rangle$ with the average value of the inductor voltage computed on a switching period, which does not allow to catch such a variation due to the phase-shift perturbation. This is illustrated in Fig. 4 by reporting with circles the values of the average quantities computed on a switching period; remarkably, the average inductor voltage computed on a switching period does not capture the variations observed in the moving average $\langle v_L \rangle$ (e.g., the negative values of $\langle v_L \rangle$), which actually have an effect on the inductor current as shown in the figure.

To overcome this limitation, a model based on the energy balance is investigated herein.

B. Energy-Based Average Model

The proposed model exploits the fact that the difference between the energy at the FSBB input and output ports must equal the variation in the inductor energy, which is related to the average inductor current on a switching period. Beginning with the input port, the energy w_g entering the port during a switching period is:

$$w_g = \int_0^{T_{sw}} V_g \, i_g(t) \, dt = V_g \int_0^{D_g T_{sw}} i_L(t) \, dt \tag{4}$$

with integration limited over the interval where the switch S_1 is conducting. In general, the current integral can be split into a contribution related to the initial current I_0 plus a remaining piecewise linear contribution:

$$\begin{aligned} w_g &= V_g \left[\frac{I_0 D_g}{f_{sw}} + \int_0^{D_g T_{sw}} i_L(t) - I_0 \, dt \right] \\ &= \frac{V_g}{f_{sw}} \left[I_0 D_g + \frac{V_g D_g^2}{2 f_{sw} L} - \frac{V_o \delta_2^2}{2 f_{sw} L} \right]. \end{aligned} \tag{5}$$

Considering the output port, the energy w_o leaving the port during a switching period is:

$$w_o = \int_0^{T_{sw}} V_o \, i_{out}(t) \, dt = V_o \int_0^{D_o T_{sw}} i_L(t - t_1) \, dt \tag{6}$$

with integration limited over the interval where the switch S_2 is conducting. In this case, the current integral is split into a contribution related to the final value I_4 plus a piecewise linear contribution:

$$\begin{aligned} w_o &= V_o \left[\frac{I_4 D_o}{f_{sw}} + \int_0^{D_o T_{sw}} i_L(t + t_1) - I_4 \, dt \right] \\ &= \frac{V_o}{f_{sw}} \left[I_4 D_o + \frac{V_o D_o^2}{2 f_{sw} L} - \frac{V_g \delta_2^2}{2 f_{sw} L} \right]. \end{aligned} \tag{7}$$

The use of the initial and final current values I_0 and I_4 allows tracking the variation of the average inductor current $\bar{i}_L$ across a switching period, as shown hereafter. From (5) and (7), it emerges that the average input and output currents are functions of the ports voltages V_g and V_o, the duty-cycles D_g and D_o, the voltage-overlap interval δ_2 and the considered current values I_0 and I_4.

The difference between the energy entering at the input port w_g and the energy leaving the output port w_o corresponds to a variation of the energy stored in the inductor Δw_L in the switching cycle. From (5) and (7), such variation results:

$$\begin{aligned} \Delta w_L &= w_g - w_o \\ &= \frac{V_g I_0 D_g - V_o I_4 D_o}{f_{sw}} + \frac{V_g^2 D_g^2 - V_o^2 D_o^2}{2 f_{sw}^2 L}. \end{aligned} \tag{8}$$

Using (2), the final value I_4 can be expressed in terms of the initial value I_0 as

$$I_4 = I_0 + \frac{V_g D_g - V_o D_o}{f_{sw} L}. \tag{9}$$

Substituting (9) in (8), it yields:

$$\Delta w_L = \frac{D_g V_g - D_o V_o}{f_{sw}} \left(I_0 + \frac{D_g V_g - D_o V_o}{2 f_{sw} L} \right). \tag{10}$$

Equation (10) shows two key components: the average voltage across the inductor in a switching period and the mean between the initial and the final inductor currents of the switching period, respectively:

$$\begin{aligned} \bar{v}_e &= D_g V_g - D_o V_o, \\ \bar{i}_e &= I_0 + \frac{D_g V_g - D_o V_o}{2 f_{sw} L} = \frac{I_0 + I_4}{2}. \end{aligned} \tag{11}$$

It is worth noting that, in (11), $\bar{i}_e$ is not equal to the average current $\bar{i}_L$ and does not take into account the phase-shift β. The current $\bar{i}_e$ may be associated with the lower or higher envelope (in the sense of lower or higher bounding function) of i_L. In the proposed modeling, $\bar{i}_e$ is considered as a new state variable for the inductor.

C. Input and Output Currents

The average input and output currents in a switching period can be derived from the energy exchanged at the respective ports. The input current $\bar{i}_g$ is given using (5) as

$$\bar{i}_g = \frac{w_g}{T_{sw} V_g} = I_0 D_g + \frac{V_g D_g^2 - V_o \delta_2^2}{2 f_{sw} L}, \tag{12}$$

while the output current $\bar{i}_{out}$ is derived from (7) as

$$\bar{i}_{out} = \frac{w_o}{T_{sw} V_o} = I_4 D_o + \frac{V_o D_o^2 - V_g \delta_2^2}{2 f_{sw} L}. \tag{13}$$

From (9) and (11), the terms I_0 and I_4 can be expressed as a function of the new variable $\bar{i}_e$, which relates these variables to the energy variation Δw_L:

$$I_{0,4} = \bar{i}_e \mp \frac{D_g V_g - D_o V_o}{2 f_{sw} L}. \tag{14}$$

Substituting (14) in (12) and (13), the input and output

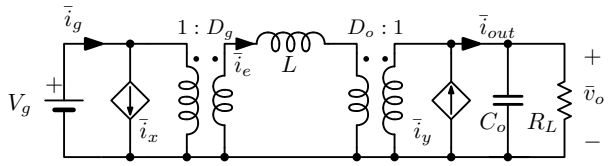

Fig. 5: Non-linear average model of the FSBB.

current equations for region $\mathcal{R}$ 4-8 can be derived:

$$\mathcal{R}\text{ 4-8}: \begin{cases} \bar{i}_g = \bar{i}_e D_g + \dfrac{V_o D_g D_o}{2 f_{sw} L} - \dfrac{V_o \delta_2^2}{2 f_{sw} L} \\ \bar{i}_{out} = \bar{i}_e D_o + \dfrac{V_g D_g D_o}{2 f_{sw} L} - \dfrac{V_g \delta_2^2}{2 f_{sw} L}. \end{cases} \tag{15}$$

The same procedure can be used for the other operating region $\mathcal{R}$ 2-6 to find the input and output average currents considering the initial current in the period I_0 as in Fig. 2a, yielding:

$$\mathcal{R}\text{ 2-6}: \begin{cases} \bar{i}_g = \bar{i}_e D_g - \dfrac{V_o D_g D_o}{2 f_{sw} L} + \dfrac{V_o \delta_2^2}{2 f_{sw} L} \\ \bar{i}_{out} = \bar{i}_e D_o - \dfrac{V_g D_g D_o}{2 f_{sw} L} + \dfrac{V_g \delta_2^2}{2 f_{sw} L}. \end{cases} \tag{16}$$

As expected, the input and output currents are functions of the overlap δ_2 and the current $\bar{i}_e$.

The input and the output currents can be represented as the sum of the current $\bar{i}_e$ multiplied by D_g and D_o, respectively, and the additional currents $\bar{i}_x$ and $\bar{i}_y$ as follows:

$$\begin{aligned} \bar{i}_g &= \bar{i}_e D_g + \bar{i}_x \\ \bar{i}_{out} &= \bar{i}_e D_o + \bar{i}_y. \end{aligned} \tag{17}$$

where these additional terms depend on the operating region:

$$\mathcal{R}\text{ 4-8}: \begin{cases} \bar{i}_x = \dfrac{V_o D_g D_o}{2 f_{sw} L} - \dfrac{V_o \delta_2^2}{2 f_{sw} L} \\ \bar{i}_y = \dfrac{V_g D_g D_o}{2 f_{sw} L} - \dfrac{V_g \delta_2^2}{2 f_{sw} L} \end{cases}$$

$$\mathcal{R}\text{ 2-6}: \begin{cases} \bar{i}_x = -\dfrac{V_o D_g D_o}{2 f_{sw} L} + \dfrac{V_o \delta_2^2}{2 f_{sw} L} \\ \bar{i}_y = -\dfrac{V_g D_g D_o}{2 f_{sw} L} + \dfrac{V_g \delta_2^2}{2 f_{sw} L}. \end{cases}$$

The resulting equivalent non-linear average model of the converter is shown in Fig. 5. Based on the relationships existing between $\bar{v}_e$, $\bar{i}_e$, $\bar{i}_g$, and $\bar{i}_{out}$, an ideal transformer is used to couple the input and output ports and the inductor L, as often done in the literature.

The linear small-signal model is derived by perturbing and linearizing the average quantities in (11) and (15)-(16). As commonly done (see, e.g., [17]), each variable is decomposed as $x = X + \hat{x}$, where X represents the steady-state component while $\hat{x}$ represents small-signal variations. Retaining only the first-order terms, the model reported in Fig. 6 yields. All the coefficients are a function of the considered operating point. The average and small-signal models, reported in Fig. 5 and Fig. 6, have the same structure in the other operating regions. Table II reports the small-signal coefficients related to Fig. 6 for the considered region.

TABLE III: List of parameters used in the simulation

Simulation Parameters			
V_g	200 V	C_o	100 µF
f_{sw}	100 kHz	D_g	0.4
R_L	20 Ω	D_o	0.6
L	6 µH	β	−0.3

IV. Simulation results

The proposed large-signal and small-signal models are verified with simulations in Matlab/Simulink using ideal components (i.e., ideal inductors, capacitors, and switches). The parameters used for the average and small-signal models are listed in Table III. If needed, parasitic elements can be included in simulations, as done, for example, considering the results reported in the next Sect. V. State-of-the-art symmetric-on-time single-update digital pulse-width modulators (DPWM) with triangular carriers are used. With such a modulation, the input control variables are D_g, D_o, and β. The derivations described in the previous Sect. II can be applied based on (1), considering the following equivalence:

$$\delta_2 = \frac{D_g + D_o + 2\beta}{2}. \tag{18}$$

A. Large-signal model validation

To verify the average model in (17), a circuit simulation using Matlab/Simulink is built comparing the responses of the proposed large-signal model in Fig. 5 and an instantaneous switching model developed in simulation. In the first simulation, a step excitation of $\Delta d = 5\%$ is applied to the control variable D_o, and the response of the output voltage V_o and the input and output currents $\bar{i}_g$ and $\bar{i}_{out}$ are compared. To excite the derived large-signal model, it is necessary to simultaneously impose also a step change of δ_2, with an amplitude of $\Delta d/2$, according to (18). In the second simulation, a step variation of $\Delta\delta = 0.2$ is applied to δ_2 to show the accuracy of the model in describing the dynamics of the input and output quantities after a change in the phase-shift. The initial circuit parameters are shown in Table III. Fig. 7 and Fig. 8 illustrate the low-frequency dynamics of the input and output currents and the output voltage responding to the D_o and δ_2 step, respectively, compared with the switching model.

The presented results show that the predicted low-frequency response of the proposed model agrees with the results provided by the instantaneous switching model.

B. Small-signal model validation

This subsection aims to verify the proposed small-signal model of the FSBB, comparing the transfer functions predicted by the model with those obtained from the frequency response measurements performed in the simulation. In particular, the analyzed transfer functions are *i)* the output duty-cycle $\hat{d}_o$ to output-voltage $\hat{v}_o$ and *ii)* the phase-shift $\hat{\beta}$ to output-voltage $\hat{v}_o$.

TABLE II: Small signal parameters of the input and the output currents in the considered regions

Region	a_g	b_g	g_g	e_g	a_o	b_o	g_o	e_o
$\mathfrak{R}$ **4-8**	$\frac{V_o D_g}{2f_{sw}L}$	$-\frac{V_o \delta_2}{f_{sw}L}$	$-\frac{\delta_2^2 - D_g D_o}{2f_{sw}L}$	$\bar{i}_e + \frac{V_o D_o}{2f_{sw}L}$	$\bar{i}_e + \frac{V_g D_g}{2f_{sw}L}$	$-\frac{V_g \delta_2}{f_{sw}L}$	$\frac{\delta_2^2 - D_g D_o}{2f_{sw}L}$	$\frac{D_o V_g}{2f_{sw}L}$
$\mathfrak{R}$ **2-6**	$-\frac{V_o D_g}{2f_{sw}L}$	$\frac{V_o \delta_2}{f_{sw}L}$	$\frac{\delta_2^2 - D_g D_o}{2f_{sw}L}$	$\bar{i}_e - \frac{V_o D_o}{2f_{sw}L}$	$\bar{i}_e - \frac{V_g D_g}{2f_{sw}L}$	$\frac{V_g \delta_2}{f_{sw}L}$	$-\frac{\delta_2^2 - D_g D_o}{2f_{sw}L}$	$-\frac{D_o V_g}{2f_{sw}L}$

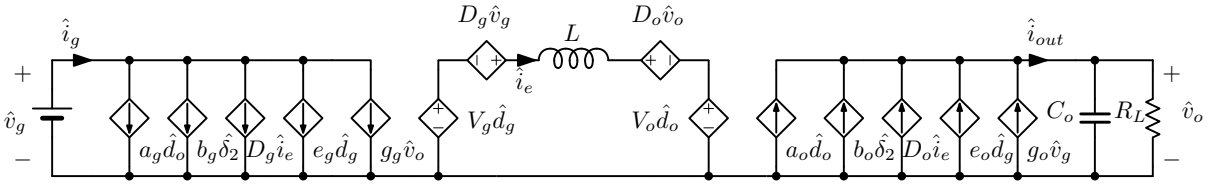

Fig. 6: Linear small-signal model of the FSBB.

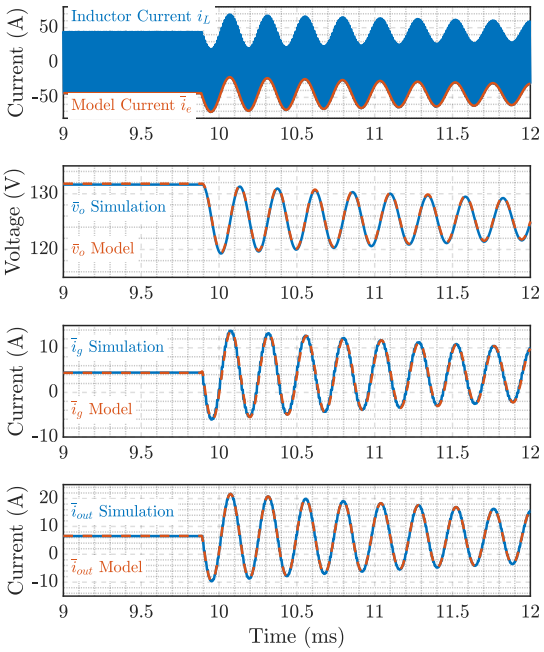

Fig. 7: Response of the switching and the proposed model to a step increment of output duty-cycle D_o of 5%. In blue the currents and voltage of the simulation, in dashed orange lines the model quantities

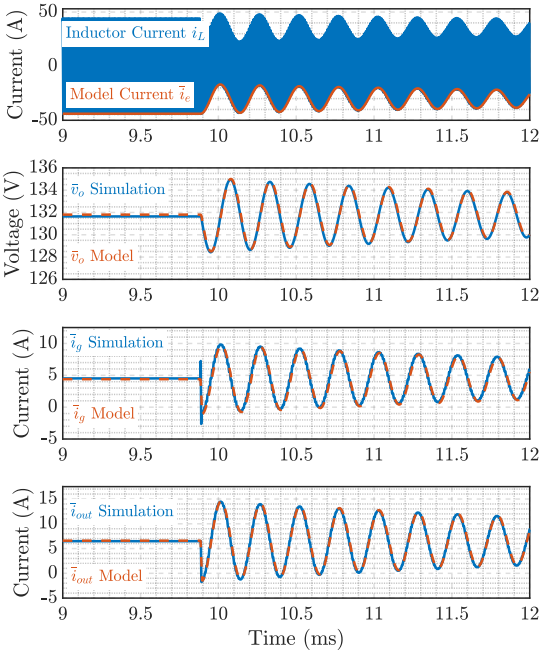

Fig. 8: Response of the switching and the proposed model to a step increment of phase-shift δ_2 of 0.2. In blue the currents and voltage of the simulation, in dashed orange lines the model quantities

The transfer function $G_{do}(s) = \hat{v}_o(s)/\hat{d}_o(s)$ is obtained setting $\hat{d}_g = \hat{v}_g = 0$ and $\hat{\delta}_2 = \hat{d}_o/2$, which stems from (18) and $\hat{\beta} = 0$; the resulting expression is:

$$G_{do}(s) = -\frac{V_o}{D_o} \frac{1 - sL\dfrac{a_o + \dfrac{b_o}{2}}{D_o V_o}}{1 + s\dfrac{L}{D_o^2 R_L} + s^2 \dfrac{LC_o}{D_o^2}}. \tag{19}$$

Simulation and experimental measurements also include the delays associated with the DPWM, which should be integrated with the theoretical $G_{do}(s)$. Let us call $G_{mod}(s)$ the transfer function between the output voltage and the perturbed modulation signal. The final overall transfer function including DPWM delays [28] is $G_{do}(s) \cdot G_{mod}(s)$, with

$$G_{mod}(s) = \frac{1}{2}\left(e^{-\frac{s(1-D_o)}{2f_{sw}}} + e^{-\frac{s(1+D_o)}{2f_{sw}}}\right) \tag{20}$$

In simulations, the perturbation of the duty-cycle is done by superimposing a sine wave to the steady-state value of D_o at different frequencies between 1 kHz and 50 kHz.

In the same way, the transfer function $G_{\delta o}(s) = \hat{v}_o(s)/\hat{\delta}_2(s)$

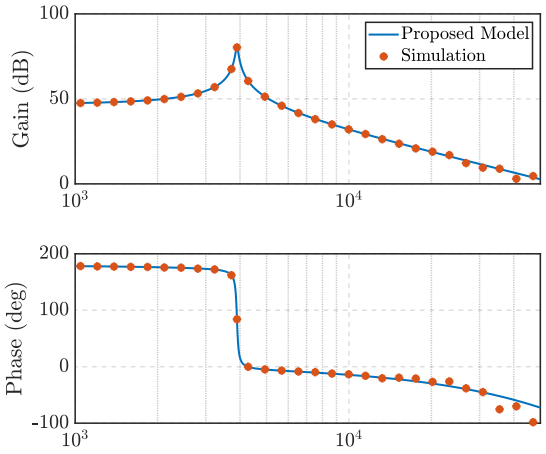

Fig. 9: Simulation validation of the output duty-cycle to output voltage transfer function. Comparison between frequency response obtained from simulations and the model $G_{do}(s) \cdot G_{mod}(s)$ in region $\mathcal{R}4$. The results are given for the following operating point: $D_g = 0.4$, $D_o = 0.6$, $\delta_2 = 0.2$.

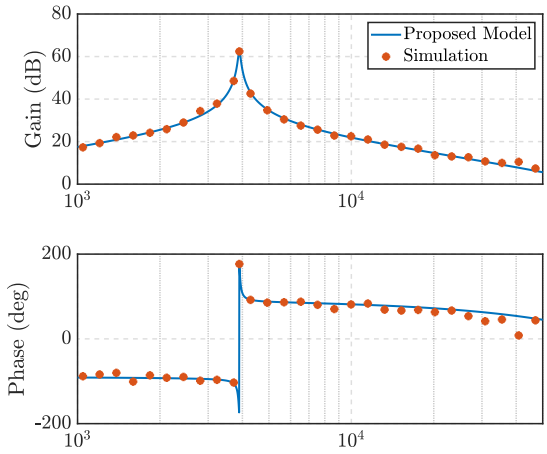

Fig. 10: Simulation validation of the phase-shift to output voltage transfer function. Comparison between frequency response obtained from simulations and the model $G_{\delta_2}(s) \cdot G_{mod}(s)$ in region $\mathcal{R}4$. The results are given for the following operating point: $D_g = 0.4$, $D_o = 0.6$, $\delta_2 = 0.2$.

can be calculated considering $\hat{d}_g = \hat{v}_g = \hat{d}_o = 0$, yielding:

$$G_{\delta o}(s) = \frac{\hat{v}_o(s)}{\hat{\delta}_2(s)} = \frac{b_o}{D_o^2} \frac{sL}{1 + s\dfrac{L}{D_o^2 R_L} + s^2 \dfrac{C_o L}{D_o^2}}. \tag{21}$$

Again, to compare the model with the simulation, the considered transfer function is $G_{\delta o}(s) \cdot G_{mod}(s)$. The perturbation of the overlap δ_2 is obtained by adding a sine wave to the steady-state reference of δ_2 in the same frequency range of the first simulation (i.e., 1 kHz and 50 kHz). From (18), δ_2 is a function of D_o, D_g and β, then the phase-shift needs to be perturbed during the sub-interval δ_4. Then, the perturbation of δ_2 corresponds only to the perturbation of the phase-shift β, avoiding unintended variation of the duty-cycles. Consequently, the update of δ_2 reference is provided by sampling the phase-shift at the end of the switching period (i.e., end of δ_4). Due to this forced sampling at the switching frequency f_{sw}, the sinusoidal characteristic of the perturbation is lost approaching the Nyquist frequency, leading to a consequent error in the frequency response.

Comparisons between simulation results and analytical predictions are shown in Fig. 9 and Fig. 10. The model accurately predicts the response across the whole considered frequency range.

The gain error between the analytical and simulated $G_{do}(s)$ transfer function is reported in Fig. 11, for all the regions. The considered frequency range is $f_r/5$ to $5f_r$ where f_r is the resonant frequency of the FSBB (i.e., $D_o/2\pi\sqrt{LC_o}$). Electrical quantities (i.e., V_g, f_{sw}, R_L, L, C_o) are given by Table III. Since δ_2 does not represent the overlap between the two voltage pulses in every region, the operating point is given in terms of D_g, D_o, and β. The models accurately predict the small-signal gain in the considered frequency range for all the regions. The maximum gain error is lower than 0.6 dB, thus validating the proposed modeling approach. Additionally,

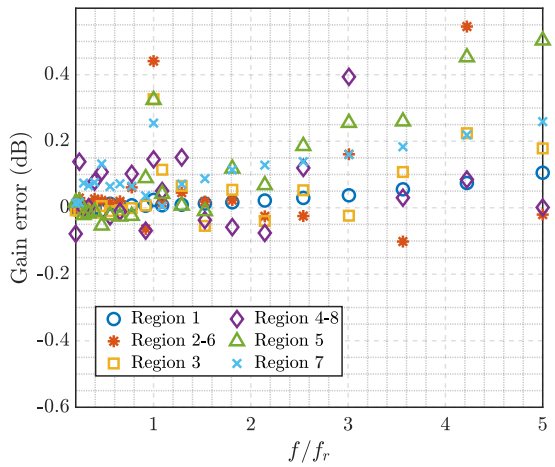

Fig. 11: Error between the analytical and simulated output duty-cycle to output voltage transfer function gain for all the regions. The results are reported for $D_g = 0.5$ and the following D_o and β: $\mathcal{R}1$: $D_o = 0.5$, $\beta = -0.05$; $\mathcal{R}2$-6:$D_o = 0.6$, $\beta = 0.3$; $\mathcal{R}3$:$D_o = 0.3$, $\beta = -0.45$; $\mathcal{R}4$-8:$D_o = 0.6$, $\beta = -0.3$; $\mathcal{R}5$:$D_o = 0.9$, $\beta = -0.15$; $\mathcal{R}7$:$D_o = 0.9$, $\beta = -0.4$; .

a comparison of the $G_{do}(s)$ transfer function between the proposed model and the standard model of the FSBB from [17] are reported in the Fig. 12. The electrical parameters are the same as before, with $D_g = 0.5$, $D_o = 0.9$ and $\delta_2 = 0.45$. The proposed model can follow the phase response, unlike the standard model in [17].

C. Control application example

A cascade control of FSBB, composed of an outer voltage control loop with an inner current control loop, is de-

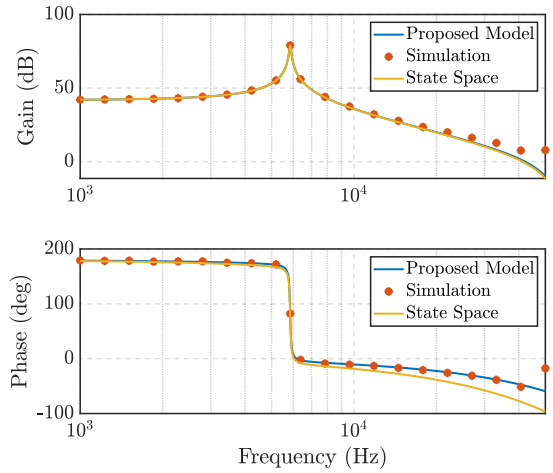

Fig. 12: Bode plots comparison of $G_{do} = \hat{v}_o/\hat{d}_o$ from proposed model, average state-space model, and simulation for $D_g = 0.5$, $D_o = 0.9$ and $\delta_2 = 0.45$.

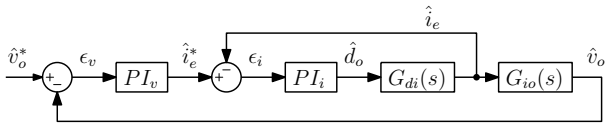

Fig. 13: Considered FSBB control structure.

signed in this section using the proposed energy model. The plant transfer functions, namely $G_{di}(s) = \hat{i}_e(s)/\hat{d}_o(s)$ and $G_{io}(s) = \hat{v}_o(s)/\hat{i}_e(s)$, are derived from Fig. 6 and reported in (22).

$$G_{di}(s) = \frac{V_o}{D_o^2 R_L} \frac{1 - \left(a_o + \frac{b_o}{2}\right)\frac{R_L D_o}{V_o} - sR_L C_o}{1 + s\frac{L}{D_o^2 R_L} + s^2 \frac{LC_o}{D_o^2}} \qquad (22)$$

$$G_{io}(s) = D_o \frac{R_L}{1 + sR_L C_o}.$$

This control is tested by imposing a step voltage variation of 5% of the output voltage reference. The current i_L is sampled at the beginning of each switching cycle, in order to acquire the desired current value $\bar{i}_e$. Remarkably, the approach does not require the information on the true average current. Parameters are listed in Table III. A lower value of the output capacitor $C_o = 15\,\mu\text{F}$ is used to consider a more critical control problem. The target phase margin is $\Phi_M = 70^\circ$, while crossover frequencies are $f_{cr}^i = 15\,\text{kHz}$ and $f_{cr}^v = f_{cr}^i/6$ (i.e., $f_{cr}^v = 2.5\text{k}\,\text{Hz}$) for current and voltage loops, respectively. The voltage reference step response is reported in Fig. 14. The figure highlights an accurate matching between the expected response of the controller designed using the proposed models and the actual response when the same designed controller is interfaced with the instantaneous simulation model of the converter.

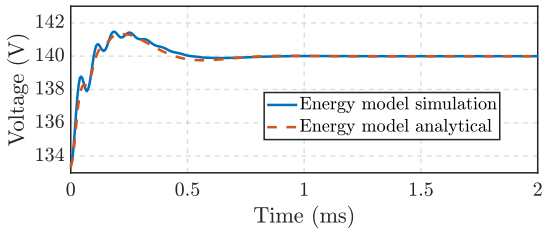

Fig. 14: Voltage reference step response of the controlled FSBB as in Fig. 13.

V. Experimental validation

To corroborate the validation performed by means of numerical simulations, additional results from experimental measurements are reported in the following. To this end, an FSBB prototype using SiC devices UJ4SC075009K4S for the input leg and UF3SC065007K4S devices for the output leg has been implemented. The inductor is based on a PQ32-N97 core with 9 turns, using $800 \times 71\,\mu\text{m}$ litz wire, and an air-gap of $1.7\,\text{mm}$. Circuit parameters are listed in Table IV. A Texas Instruments microcontroller TMS320F28379D is used to implement the DPWM.

Fig. 15 displays the experimentally obtained time-domain waveforms of the input and output switching node voltage v_1 and v_2, and inductor current i_L of the tested FSBB in the region $\mathcal{R}8$; the considered operating point is $V_g = 50\text{V}$, $f_{sw} = 100\,\text{kHz}$, $D_g = 0.5$, $D_o = 0.6$, $\delta_2 = 0.3$. Frequency response measurements were performed to experimentally validate the transfer function from the output duty-cycle to the output voltage. To this end, the Bode functionality of the Rohde&Schwartz RTA4004 oscilloscope was used, which computes the Bode plot considering the signals applied at two input channels of the oscilloscope as input and output variables. The waveform generator signal of the RTA4004 is used to stimulate the system to be characterized by a series of tones at specified frequencies. In this case, the stimulus signal is given as input to the microcontroller TMS320F28379D and, after proper filtering and scaling, used to impress the sinusoidal perturbations on the modulation variables (e.g., the duty-cycle of the output leg). This signal is considered as input for the generation of the Bode plot, while the output voltage V_o of the FSBB is considered as output. The Bode plot measurement procedure is performed through the following steps:

- Calibration: by connecting the two probes together, the measurement offset, which will later be subtracted from the main results, is measured;
- Measurement: using the Bode application, the frequency response of the target transfer function is measured;
- Post-processing: the results from the previous step are post-processed, taking into consideration the microcontroller operation and subtracting the offset calculated from the calibration step.

These steps are applied for the experimental measurement of the transfer function among the perturbed modulation signal and the output voltage.

TABLE IV: Parameter values of the circuit

V_g	50 V	C_o	25 µF
f_{sw}	100 kHz	R_{ind}	120 mΩ
R_L	45.6 Ω	R_C	20 mΩ
L	6.4 µH	t_d	120 ns

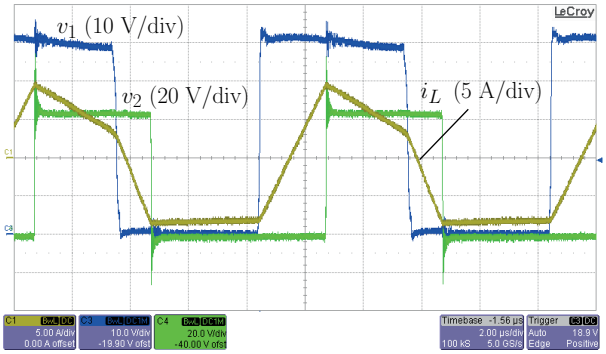

Fig. 15: Input and output switching node voltage v_1 and v_2, and inductor current i_L of two operating points: (a) $D_g = 0.5$, $D_o = 0.4$, $\delta_2 = 0.23$.

The experimental measurements are compared in the following with results obtained analytically and in simulation. Parasitic elements present in the experimental setup are taken into account in the models used in this section, which include inductor resistance R_{ind}, MOSFETs on-resistance R_{dson}, capacitor ESR R_C, and dead-times t_d. In the simulation model, parasitic resistances are added in series with the corresponding elements (e.g., inductors, switches, etc), while the dead-time effect is included by delaying the rising edges of all of the MOSFETs' gate signals. The proposed analytical model is also enhanced to include the aforementioned non-idealities. For example, the circuit model in Fig. 6 is modified by adding the resistances related to the inductor, the MOSFETs, and the capacitor losses in series with the respective circuit elements. On this basis, the impedances of inductance and capacitance become $Z_L = sL + R_{ind} + R_{dson1} + R_{dson2}$ and $Z_{out} = 1/sC_o + R_C$, respectively, where R_{dson1} and R_{dson2} are the on-resistances of the first and second leg. This yields the following output duty-cycle to output voltage transfer function:

$$G_{do}^{par}(s) = \frac{\hat{v}_o(s)}{\hat{d}_o(s)} = Z_{out}\frac{a_o + \dfrac{b_o}{2} - \dfrac{D_o V_o}{Z_L}}{1 + \dfrac{D_o^2 Z_{out}}{Z_L}} \tag{23}$$

The dead-time is taken into account as a reduction of the effective duty-cycles D_g and D_o.

Comparison results between the proposed small-signal model taking into account converter non-idealities and the previously explained experimental and simulated frequency response measurements, are provided in Fig. 16 for the step-up and step-down case. Simulation results match the analytical

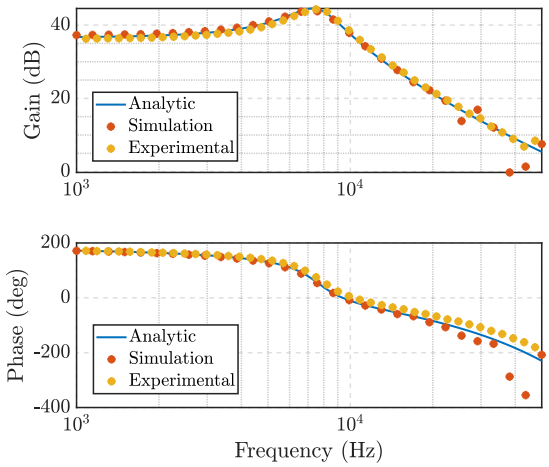

Fig. 16: Verification of the output duty-cycle to output voltage transfer function. Comparison between frequency response obtained from simulations, experimental results and model $G_{do}^{par}(s) \cdot G_{mod}(s)$. The results are given for the operating point: $D_g = 0.5$, $D_o = 0.4$, $\delta_2 = 0.23$.

predictions in the whole considered frequency range. Around the resonant frequency, a small mismatch is observed in the experimental results. This is assumed to be related to the non-linear effect of the dead-times, as reported in [29], of the core [30], and of the switching losses [31].

VI. Conclusion

This paper has presented a non-linear average model and the corresponding small-signal model of the four-switch buck-boost converter under both duty-cycle and phase-shift modulation. This paper focused on two specific regions of operation that allow zero voltage switching of all four switches, the same model procedure can be used for the other operating region. In the presented modelling approach, the average inductor current is not one of the state variables, and instead, a new state variable based on the inductor energy variations is introduced. The model allows the implementation of current control based on the sampling of the initial current at the beginning of the switching period. This avoids post-processing computation or low-pass filters to sense the average current. The simulation and experimental results have verified the non-linear large-signal and linearized small-signal models of the four-switch buck-boost converter for both duty-cycle and phase-shift variations.

References

[1] X. Sun *et al.*, "An improved wide input voltage buck-boost + LLC cascaded converter," in *2015 IEEE Energy Conversion Congress and Exposition (ECCE)*, 2015, pp. 1473–1478.

[2] Y. Li and X. Ruan, "An optimized inductor current control for intermediate bus converter with hybrid-switching structure," in *2018 IEEE Energy Conversion Congress and Exposition (ECCE)*, 2018, pp. 3818–3824.

[3] Z. Wang *et al.*, "A high efficiency and high power density integrated two-stage DC-DC converter based on bipolar symmetric phase shift modulation strategy," *IEEE Transactions on Power Electronics*, vol. 37, no. 4, pp. 4358–4373, apr 2022.

[4] N. Zanatta *et al.*, "Design and implementation of a two-stage resonant converter for wide output range operation," *IEEE Transactions on Industry Applications*, vol. 58, no. 6, pp. 7457–7468, nov 2022.

[5] Z. Wang *et al.*, "A high-efficiency and high-power-density interleaved integrated buck-boost-llc converter and its comprehensive optimal design method," *IEEE Transactions on Power Electronics*, vol. 37, no. 9, pp. 10 849–10 863, sep 2022.

[6] C. Xu *et al.*, "A novel converter integrating buck-boost and DAB converter for wide input voltage," in *IECON 2020 The 46th Annual Conference of the IEEE Industrial Electronics Society*. IEEE, oct 2020.

[7] M. Fu *et al.*, "A two-stage rail grade DC/DC converter based on GaN device," in *2019 IEEE Applied Power Electronics Conference and Exposition (APEC)*. IEEE, mar 2019.

[8] Z. Wang *et al.*, "GaN devices based integrated two-stage DC-DC converter with voltage regulation," in *2020 IEEE Applied Power Electronics Conference and Exposition (APEC)*. IEEE, mar 2020.

[9] S. Mukherjee *et al.*, "A two-stage automotive LED driver with multiple outputs," *IEEE Transactions on Power Electronics*, vol. 36, no. 12, pp. 14 175–14 186, dec 2021.

[10] Z. Ye *et al.*, "A two-stage resonant inverter with control of the phase angle and magnitude of the output voltage," *IEEE Transactions on Industrial Electronics*, vol. 54, no. 5, pp. 2797–2812, oct 2007.

[11] W. Lujun *et al.*, "Efficient and fast active equalization method for retired battery pack using wide voltage range bidirectional converter and DBSCAN clustering algorithm," *IEEE Transactions on Power Electronics*, vol. 37, no. 11, pp. 13 824–13 833, nov 2022.

[12] A. J. Hanson and D. J. Perreault, "A high-frequency power factor correction stage with low output voltage," *IEEE Journal of Emerging and Selected Topics in Power Electronics*, vol. 8, no. 3, pp. 2143–2155, 2020.

[13] Q. Tian *et al.*, "Symmetric bipolar output full-bridge four-port converter with phase-shift modulated buck–boost voltage balancer," *IEEE Transactions on Industrial Electronics*, vol. 69, no. 8, pp. 8040–8054, 2022.

[14] L. L. O. Carralero *et al.*, "PV emulator based on a four-switch buck-boost DC-DC converter," in *2019 IEEE 15th Brazilian Power Electronics Conference and 5th IEEE Southern Power Electronics Conference (COBEP/SPEC)*. IEEE, dec 2019.

[15] M. Orellana *et al.*, "Four switch buck-boost converter for photovoltaic DC-DC power applications," in *IECON 2010 - 36th Annual Conference on IEEE Industrial Electronics Society*. IEEE, nov 2010.

[16] J.-K. Shiau *et al.*, "Stability analysis of a non-inverting synchronous buck-boost power converter for a solar power management system," in *2008 IEEE International Conference on Sustainable Energy Technologies*. IEEE, nov 2008.

[17] R. W. Erickson and D. Maksimovic, *Fundamentals of Power Electronics*, 2nd ed. Springer, 2020.

[18] S. Waffler and J. W. Kolar, "A novel low-loss modulation strategy for high-power bidirectional buck + boost converters," *IEEE Transactions on Power Electronics*, vol. 24, no. 6, pp. 1589–1599, 2009.

[19] Y. Bai *et al.*, "A simplified quadrangle current modulation for four-switched buck-boost converter (fsbb) with a novel small signal model," in *2023 IEEE Applied Power Electronics Conference and Exposition (APEC)*, 2023, pp. 736–743.

[20] X. Ren *et al.*, "Three-mode dual-frequency two-edge modulation scheme for four-switch buck–boost converter," *IEEE Transactions on Power Electronics*, vol. 24, no. 2, pp. 499–509, 2009.

[21] H. Xu *et al.*, "Short-time scale mode transition control of the four-switch buck-boost converter," in *2021 11th International Conference on Power and Energy Systems (ICPES)*, 2021, pp. 62–67.

[22] C.-W. Chen *et al.*, "Modeling and controller design for a four-switch buck-boost converter in distributed maximum power point tracking PV system applications," in *2012 IEEE Energy Conversion Congress and Exposition (ECCE)*. IEEE, sep 2012.

[23] S. Chakraborty *et al.*, "Approaches for continuous-time dynamic modeling of the asymmetric dual-active half-bridge converter," in *2018 IEEE Applied Power Electronics Conference and Exposition (APEC)*, 2018, pp. 952–958.

[24] H. Daneshpajooh *et al.*, "Modeling of the Phase Shift plus Duty Cycle Controlled Half Bridge DC to DC Converter," in *Intelec 2013; 35th International Telecommunications Energy Conference, SMART POWER AND EFFICIENCY*, 2013, pp. 1–6.

[25] F. Gao *et al.*, "Average Modeling of a Dual-Half-Bridge Converter Modulated With Three Degrees of Freedom," *IEEE Transactions on Transportation Electrification*, vol. 7, no. 3, pp. 1016–1030, 2021.

[26] J. Kim *et al.*, "Asymmetric Duty Control of a Dual-Half-Bridge DC/DC Converter for Single-Phase Distributed Generators," *IEEE Transactions on Power Electronics*, vol. 26, no. 3, pp. 973–982, 2011.

[27] E. Gallo *et al.*, "Average and small-signal model of the four-switch buck-boost converter under both duty-cycle and phase-shift modulation," in *2023 IEEE Applied Power Electronics Conference and Exposition (APEC)*, 2023, pp. 1299–1306.

[28] D. Van de Sype *et al.*, "Small-signal laplace-domain analysis of uniformly-sampled pulse-width modulators," in *2004 IEEE 35th Annual Power Electronics Specialists Conference (IEEE Cat. No.04CH37551)*, vol. 6, 2004, pp. 4292–4298 Vol.6.

[29] M. Berg *et al.*, "Deadtime impact on the small-signal output impedance of single-phase power electronic converters," in *2019 20th Workshop on Control and Modeling for Power Electronics (COMPEL)*, 2019, pp. 1–8.

[30] P. Wilson *et al.*, "Modeling frequency-dependent losses in ferrite cores," *IEEE Transactions on Magnetics*, vol. 40, no. 3, pp. 1537–1541, may 2004.

[31] A. Ayachit and M. K. Kazimierczuk, "Averaged small-signal model of PWM DC-DC converters in CCM including switching power loss," *IEEE Transactions on Circuits and Systems II: Express Briefs*, vol. 66, no. 2, pp. 262–266, feb 2019.

Ezio Gallo received the M.S. degree in Electronics engineering from the University of Padova, Padova, Italy in 2020. He is currently working toward the Ph.D. degree in mechatronics and product innovation engineering with the Department of Management and Engineering, University of Padova, Vicenza, Italy. His research interests are oriented to the analysis, design and optimization of dc dc power electronic converter.

Davide Biadene (S'11–M'21) received the M.S. degree in electronic engineering and the Ph.D. degree in information engineering from the University of Padova, Padova, Italy, in 2014 and 2017, respectively. He is currently a research fellow at the Department of Management and Engineering, University of Padova, Vicenza, Italy. He was a visiting Ph.D. student with the Power Electronic Systems Laboratory, Department of Information Technology and Electrical Engineering, ETH Zurich, Zurich, Switzerland, in 2016. From 2017 to 2021 he was with Infineon Technologies Italia, employed as an R&D test engineer in the automotive business line team. His current research interests include dc-dc converters for renewables and energy storage devices.

Filip Cvejić was born in Belgrade, Serbia in 1996. He received the B.S. and M.S. degrees in electrical engineering from the University of Belgrade, Belgrade, Serbia, in 2019 and 2021, respectively. He has worked in research and development of various companies, as well as a researcher at the Department of Information Engineering of University of Padova. He is currently employed at Invenda Solutions, Novi Sad, Serbia. Mr. Cvejić received the IEEE 2019 International Future Energy Challenge Grand Award as part of the H-Bridges team.

Giorgio Spiazzi received the graduation degree (cum laude) in electronic engineering and the Ph.D. degree in industrial electronics and informatics from the University of Padova, Padova, Italy, in 1988 and 1993, respectively.,He is currently a Full Professor with the Department of Information Engineering (DEI), University of Padova. His main research interests include dc–dc converters for renewable energy sources, high-power-factor rectifiers, soft-switching techniques, solid-state lamp ballasts, and electromagnetic compatibility in power electronics.

Tommaso Caldognetto received the M.S. (Hons.) degree in electronic engineering and the Ph.D. degree in information engineering from the University of Padova, Padova, Italy, in 2012 and 2016, respectively. He currently works as an Assistant Professor at the University of Padova, Italy. His research activities are in the area of electronics engineering, specifically in power electronics. Dr. Caldognetto published several journal and conference papers on the topic of grid-tied converters control and management of distributed energy resources in intelligent power systems (e.g., microgrids). Dr. Caldognetto is currently a member of the IEEE Power Electronics Society and an Associate Editor for the IEEE Open Journal of Power Electronics. He is a Senior Member of the IEEE.